

# Effects of collisional ion orbit loss on neoclassical tokamak radial electric fields

Hongxuan Zhu, T. Stoltzfus-Dueck, R. Hager, S. Ku, and  
C. S. Chang

Princeton Plasma Physics Laboratory, Princeton, NJ 08543, USA

**Abstract.** Ion orbit loss is considered important for the radial electric field  $E_r$  in tokamak edge plasmas. In neoclassical equilibria, collisions can scatter ions onto loss orbits and generate a steady-state radial current. The latter could potentially drive the edge  $E_r$  away from its neoclassical value. To quantitatively measure this effect, an ion-orbit-flux diagnostic has been implemented in the axisymmetric version of the gyrokinetic particle-in-cell code XGC. The validity of the diagnostic is demonstrated by studying the collisional relaxation of  $E_r$  in the core plasma. After this verification, the ion orbit-loss effect is numerically measured in the edge for an H-mode plasma in DIII-D geometry. In quasisteady state, the edge  $E_r$  is found to be mainly determined by the radial ion force balance condition, in which the radial electric force on ions balances the large ion pressure gradient associated with the given density pedestal. In this quasisteady state, the collisional orbit-loss effect cannot drive  $E_r$  significantly away from its neoclassical value.

## 1. Introduction

In tokamaks, the ion orbits have finite excursion widths across magnetic flux surfaces, so the ions at the plasma edge can move across the last closed flux surface (LCFS) and enter the scrape-off-layer (SOL) region. While some ions will cross the LCFS again and return to the confined region, others may hit the wall. This effect is known as ion orbit loss, and is considered important for the modeling of plasma properties at the edge such as the radial electric field  $E_r$  and the toroidal rotation. The effect of ion orbit loss has been studied by many authors [1, 2, 3, 4, 5, 6, 7, 8, 9, 10], and it is often assumed that the ion distribution function is empty at the loss-orbit region but is otherwise Maxwellian [11, 12, 13]. However, this assumed distribution function is unlikely to be achieved in a steady state, posing questions on the relevance of the theory. Also, in the presence of a magnetic X point (figure 1), the ion-orbit-loss effect is popularly believed to be stronger for the “forward- $\nabla B$ ” configuration when the magnetic drift points towards the X point, compared to the “backward- $\nabla B$ ” configuration when the magnetic drift points away from the X point [14, 15, 16]. But quantitative evaluation of this effect between the two configurations are still required.

In this paper, we study the quantitative effects of ion orbit loss on the neoclassical  $E_r$  by considering the following well posed problem. In a steady state, the total radial current  $J_r = J_{\text{vis}} + J_{\text{loss}}$  must be equal to zero, where  $J_{\text{vis}}$  is induced by the neoclassical viscosity and  $J_{\text{loss}}$  is induced by the steady-state collisional scattering onto the loss orbits. Absent ion orbit loss,  $J_{\text{vis}} = 0$  corresponds to the neoclassical solutions of  $E_r$ . When the ion orbit-loss effect becomes important, from the relation  $J_{\text{vis}} = -J_{\text{loss}}$ , one can evaluate how  $J_{\text{loss}}$  drives  $E_r$  away from its neoclassical value [12, 14, 17, 18]. Further, by comparing  $J_{\text{loss}}$  between the forward- and backward- $\nabla B$  configurations, one can quantitatively study how ion orbit loss depends on the direction of the magnetic drift.

To measure  $J_{\text{loss}}$ , we have implemented a new numerical diagnostic in the gyrokinetic particle-in-cell code XGC [19]. This diagnostic is based on the recently proposed ion-orbit-flux formulation [20, 21], which allows us to measure the separate contributions to the ion orbit loss from different transport mechanisms and sources. To focus on the neoclassical physics where  $J_{\text{loss}}$  is caused solely by collisional transport, we report results from electrostatic simulations using the axisymmetric version of XGC (XGCa) in this paper. We first demonstrate the validity of our diagnostic by studying the collisional relaxation of  $E_r$  in the core. Then, we numerically measure  $J_{\text{loss}}$  at the edge for an H-mode plasma in the DIII-D geometry. In quasisteady state, the edge  $E_r$  is found to be mainly

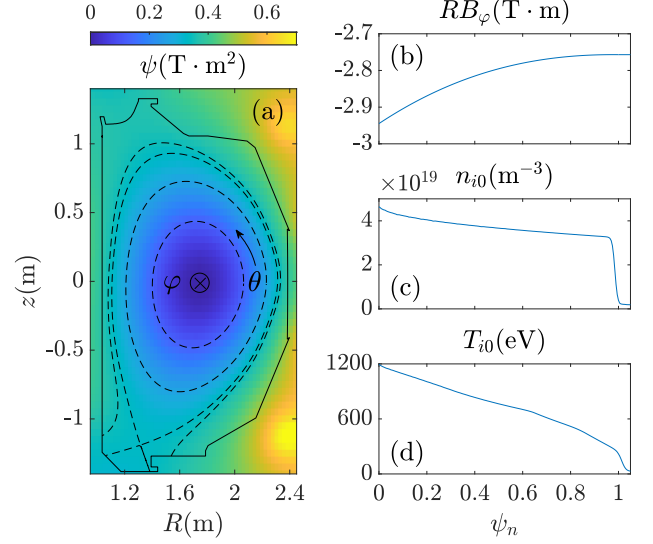


**Figure 1.** (a): The poloidal flux  $\psi$  (shown by the color) from the DIII-D shot 141451 [22, 23, 24]. The dashed curves show several flux surfaces and the solid curve is the wall. Cylindrical coordinates  $(R, \varphi, z)$  are used. We choose the poloidal angle  $\theta$  to increase counterclockwise. (b-d): The equilibrium  $I = RB_\varphi$ , ion density  $n_{i0}$ , and ion temperature  $T_{i0}$  versus the normalized flux  $\psi_n \doteq (\psi - \psi_a)/(\psi_X - \psi_a)$ , where  $\psi_a$  and  $\psi_X$  are the value of  $\psi$  at the magnetic axis and the X point, respectively.

determined by the radial ion force balance condition, in which the radial electric force on ions balances the large ion pressure gradient associated with the given density pedestal. In this quasisteady state, the collisional orbit-loss effect cannot drive  $E_r$  significantly away from its neoclassical value. We emphasize that this conclusion only applies to the quasisteady state, when  $E_r$  is already fully developed against the given density pedestal. Ion orbit loss has been found to play a much more significant role during transient states, such as the development of the density pedestal itself [14]. Effects from ion orbit loss during transient states are beyond the scope of this article.

The rest of the paper is organized as follows. Section 2 describes the setup for the XGCa simulations and the implementation of the ion-orbit-flux diagnostic. Section 3 studies the collisional relaxation of  $E_r$  at the core. Section 4 studies the effects of ion orbit loss on  $E_r$  at the edge. Conclusions are given in section 5.

## 2. XGCa simulation setup and ion-orbit-flux diagnostic implementation

### 2.1. XGCa simulation setup

We use electrostatic XGCa simulations to study an axisymmetric H-mode plasma in DIII-D geometry, with the plasma equilibrium from shot 141451 [22, 23, 24]. The code uses cylindrical coordinates  $\mathbf{R} \doteq (R, \varphi, z)$  to describe the realistic toroidal geometry

containing an X point (figure 1 (a)). The equilibrium magnetic field is given by  $\mathbf{B} = I(\psi)\nabla\varphi + \nabla\psi \times \nabla\varphi$ , where  $\psi$  is the poloidal magnetic flux and  $I = RB_\varphi$  is a flux function. Since  $B_\varphi < 0$  (figure 1(b)), the ion magnetic drift points in the negative- $z$  direction, which is the forward- $\nabla B$  configuration. We will also simulate the backward- $\nabla B$  configuration where the sign of  $B_\varphi$  is reversed ( $B_\varphi > 0$ ), while all other signs are kept the same. The poloidal flux  $\psi$  increases radially, so the poloidal magnetic field  $B_\theta$  is positive. If one reverses the sign of  $B_\theta$  while keeping  $B_\varphi$  unchanged, then the plasma will behave the same except that the toroidal-rotation direction is reversed. The code utilizes unstructured triangular meshes, with most of the nodes aligned with flux surfaces [25]. For our simulations, the mesh has a radial grid size of  $\Delta\psi_n \approx 0.004$  and a poloidal grid size of  $\Delta l_\theta \approx 1\text{cm}$ . The normalized flux is defined as  $\psi_n \doteq (\psi - \psi_a)/(\psi_X - \psi_a)$ , where  $\psi_a$  and  $\psi_X$  are the value of  $\psi$  at the magnetic axis and the X point, respectively.

We simulate deuterium ions with mass  $m_i = 2m_p$  and charge number  $Z_i = 1$ , where  $m_p$  is the proton mass. The equilibrium ion density  $n_{i0}(\psi)$  and temperature  $T_{i0}(\psi)$  are functions only of  $\psi$ , and are shown in figures 1(c) and 1(d). The ion gyrocenter coordinates are position  $\mathbf{R}$ , magnetic moment  $\mu$ , and parallel momentum  $p_\parallel$ . Their characteristics are governed by equations given in Ref. [26], which are mathematically equivalent to the following:

$$B_\parallel^* \dot{\mathbf{R}} = (Z_i e)^{-1} \hat{\mathbf{b}} \times \nabla H + v_\parallel \mathbf{B}^*, \quad (1)$$

$$B_\parallel^* \dot{p}_\parallel = -\mathbf{B}^* \cdot \nabla H, \quad (2)$$

and  $\dot{\mu} = 0$ . Here, the overhead dot denotes the time derivative,  $\hat{\mathbf{b}} \doteq \mathbf{B}/B$ ,  $\mathbf{B}^* \doteq \mathbf{B} + \nabla \times (p_\parallel \hat{\mathbf{b}}/Z_i e)$ ,  $B_\parallel^* \doteq \hat{\mathbf{b}} \cdot \mathbf{B}^*$ ,  $H = p_\parallel^2/2m_i + \mu B + Z_i e \hat{J}_0 \Phi$  is the gyrocenter Hamiltonian,  $v_\parallel \doteq \partial_{p_\parallel} H$  is the parallel velocity,  $e$  is the elementary charge,  $\hat{J}_0$  is the gyroaverage operator, and  $\Phi$  is the electrostatic potential. Note that  $v_\parallel = p_\parallel/m_i$  for the present electrostatic formulations.

Using the the “total-f” simulation method [27], the code calculates both the ion orbits and ions’ distribution function  $F_i(\mathbf{R}, \mu, p_\parallel, t)$ . The distribution function is chosen to be Maxwellian at the beginning of the simulation:

$$F_i|_{t=0} = n_{i0} \left( \frac{m_i}{2\pi T_{i0}} \right)^{3/2} e^{-(p_\parallel^2/2m_i + \mu B)/T_{i0}}. \quad (3)$$

At  $t > 0$ , the ion marker’s weights are adjusted such that  $F_i$  evolves in time according to

$$d_t F_i \doteq \partial_t F_i + \dot{\mathbf{R}} \cdot \nabla F_i + \dot{p}_\parallel \partial_{p_\parallel} F_i = C_i + S_i. \quad (4)$$

Here,  $C_i$  is a nonlinear Fokker–Planck–Landau collision operator [28, 29] and  $S_i$  represents source (such as neutral ionization) and sink. In our simulations, only the effects from  $C_i$  are retained, while  $S_i$  is assumed

to be zero. The wall perfectly absorbs ions. This is done by flipping the sign of  $p_\parallel$  for the ion markers that hit the wall and changing their weights such that the outgoing  $F_i = 0$  [9].

Let us define the velocity-space integration as

$$\int d\mathcal{W} \doteq (2\pi/m_i^2) \int d\mu dp_\parallel B_\parallel^*. \quad (5)$$

The ion-density perturbation is then  $\delta n_i \doteq \int d\mathcal{W} F_i - n_{i0}$ , and  $\Phi$  can be calculated from the gyrokinetic Poisson equation (with  $Z_i = 1$ ):

$$\nabla_\perp \cdot \left( \frac{n_{i0} m_i}{e B^2} \nabla_\perp \Phi \right) = -(\hat{J}_0 \delta n_i - \delta n_e), \quad (6)$$

where  $\nabla_\perp$  denotes gradient perpendicular to  $\mathbf{B}$ . For the electron-density perturbation  $\delta n_e$ , we adopt the adiabatic-electron model, which assumes

$$\frac{\delta n_e}{n_{e0}} = \frac{e}{T_{e0}} (\Phi - \langle \Phi \rangle). \quad (7)$$

Here,  $n_{e0}(\psi)$  and  $T_{e0}(\psi)$  are the equilibrium electron density and temperature, respectively. We have  $n_{e0} = n_{i0}$  from charge neutrality, and it is assumed that  $T_{e0} = T_{i0}$ . Also,  $\langle \dots \rangle \doteq \int (\dots) \sqrt{g} d\theta / \int \sqrt{g} d\theta$  is the flux-surface average, where  $\sqrt{g} \doteq (\nabla\psi \times \nabla\varphi \cdot \nabla\theta)^{-1}$  is the Jacobian, and the integration over  $\varphi$  is omitted due to the axisymmetry in XGCa. Note that for the SOL region, the flux-surface average is performed along open (rather than closed) field lines.

When solving the gyrokinetic Poisson equation (6), the boundary condition is  $\Phi = 0$  at the wall, at the private-flux region below the X point, and where  $\psi_n > \psi_{\text{bdry}}$ . For the results presented in this article, we chose  $\psi_{\text{bdry}} = 1.04$ , but we also found that  $E_r$  inside the LCFS is insensitive to the value of  $\psi_{\text{bdry}}$ , as long as it is not too close to unity. Since we used the adiabatic-electron model (7), realistic electron dynamics and the sheath-boundary effects in the SOL are not included in our simulations. Kinetic electrons and sheath models should be included in order to properly account for these effects [9]. Nevertheless, the present adiabatic-electron simulations suffice to model quasisteady  $E_r$  inside the LCFS, which we found to be insensitive to the dynamics in the SOL.

The electron radial current vanishes with the adiabatic-electron model (7). Then, the ion radial current must also vanish due to the quasineutrality constraint. Therefore, to avoid confusion, we look at the ion radial gyrocenter flux  $\Gamma_r$  rather than the actual radial current  $J_r$  in the rest of the paper. Note that although  $\Gamma_r$  can be nonzero, physically it is always balanced by the classical polarization flux, which corresponds to the left-hand side of the gyrokinetic Poisson equation (6). This ensures that the ion radial current is zero and the plasma is quasineutral.

Finally, we mention that our simulation setup is similar to a previous study of the plasma edge rotation

using an earlier version of the code [30]. As will be shown in section 4.3, results on the edge rotation from our simulations are similar to those reported in reference [30]. However, since the edge rotation is not central to our study, we do not make further quantitative comparisons.

## 2.2. Ion-orbit-flux diagnostic implementation

The ion-orbit-flux formulation uses the coordinates  $(\mu, \mathcal{P}_\varphi, \bar{H})$  to label ion orbits that cross the LCFS, where  $\mathcal{P}_\varphi \doteq Z_i e \psi + p_\parallel \hat{\mathbf{b}} \cdot R^2 \nabla \varphi$  is the canonical toroidal angular momentum and  $\bar{H}$  is a chosen “orbit Hamiltonian” [20, 21]. The formulation is exact with any time-dependent  $\bar{H}$ , provided  $\bar{H}$  is axisymmetric. Therefore, we may choose  $\bar{H}$  to be the toroidal average of  $H$ , i.e.,  $\bar{H} = \oint d\varphi H / 2\pi$ . For XGCa, one straight-forward choice is  $\bar{H} = H$ , but we will also make alternate choices to illustrate the formalism (section 3.2). The corresponding orbit characteristics are given by

$$B_\parallel^* \bar{\mathbf{R}} = (Z_i e)^{-1} \hat{\mathbf{b}} \times \nabla \bar{H} + \bar{v}_\parallel \mathbf{B}^*, \quad (8)$$

$$B_\parallel^* \bar{\mathbf{p}}_\parallel = -\mathbf{B}^* \cdot \nabla \bar{H}, \quad (9)$$

with  $\bar{v}_\parallel \doteq \partial_{p_\parallel} \bar{H}$ . One can also define the “remainder” Hamiltonian  $\tilde{H} \doteq H - \bar{H}$  and the corresponding quantities

$$B_\parallel^* \tilde{\mathbf{R}} = (Z_i e)^{-1} \hat{\mathbf{b}} \times \nabla \tilde{H} + \tilde{v}_\parallel \mathbf{B}^*, \quad (10)$$

$$B_\parallel^* \tilde{\mathbf{p}}_\parallel = -\mathbf{B}^* \cdot \nabla \tilde{H}, \quad (11)$$

with  $\tilde{v}_\parallel \doteq \partial_{p_\parallel} \tilde{H}$ . Let us define an orbit derivative at fixed time,  $\bar{d}_o \doteq \bar{\mathbf{R}} \cdot \nabla + \bar{\mathbf{p}}_\parallel \partial_{p_\parallel}$  [21], then, (4) becomes

$$\bar{d}_o F_i = -\tilde{\mathbf{R}} \cdot \nabla F_i - \tilde{\mathbf{p}}_\parallel \partial_{p_\parallel} F_i + C_i + S_i - \partial_t F_i. \quad (12)$$

Note that (12) is exactly equivalent to (4), and we do not require  $\tilde{H}$  to be much smaller than  $\bar{H}$ . The orbits  $(\bar{\mathbf{R}}(\tau), \bar{\mathbf{p}}_\parallel(\tau))$ , parameterized by  $\mu$ , are obtained by integrating (8) and (9) over a timelike variable  $\tau$  at fixed true time  $t$ . It is straightforward to show that  $\bar{H}$  and  $\mathcal{P}_\varphi$  are constant along the orbits [21], namely,

$$\bar{d}_o \bar{H} = \bar{d}_o \mathcal{P}_\varphi = 0. \quad (13)$$

Therefore, the orbits can be labeled by  $(\mu, \mathcal{P}_\varphi, \bar{H})$ , and they must form closed loops on the 2-dimensional plane  $(r, z)$  [21]. This means that any orbit that leaves the LCFS must have also entered it earlier.

From a coordinate transformation, the radial ion gyrocenter orbit flux through the LCFS can be expressed as [20]

$$\Gamma_r \doteq \int d\mathbf{S} \cdot \int d\mathcal{W} F_i \bar{\mathbf{R}} = \frac{2\pi}{Z_i e m_i^2} \times \int_0^\infty d\mu \int_{-\infty}^\infty d\mathcal{P}_\varphi \sum_k \int_{\bar{H}_k^{\min}}^{\bar{H}_k^{\max}} d\bar{H} \oint d\varphi (F_i^{\text{out}} - F_i^{\text{in}}). \quad (14)$$

Here,  $d\mathbf{S} \doteq \sqrt{g} d\theta d\varphi \nabla \psi$  is the surface element. The range of  $\bar{H}$  is determined by varying  $\theta$  from 0 to  $2\pi$  at fixed  $\mu$  and  $\mathcal{P}_\varphi$ , and  $k$  labels the local minimum and maximum of  $\bar{H}(\theta)$ . For a given orbit,  $F_i^{\text{in}}$  and  $F_i^{\text{out}}$  are evaluated at the incoming and the outgoing points where the orbit crosses the LCFS. The difference between  $F_i^{\text{in}}$  and  $F_i^{\text{out}}$  can be calculated by integrating the orbit derivative along the orbits, i.e.,

$$F_i^{\text{out}} - F_i^{\text{in}} = \int_0^{\tau_{\text{orb}}} d\tau \bar{d}_o F_i. \quad (15)$$

Then, we have our ion-orbit-flux formulation ready for numerical evaluations:

$$\Gamma_r = \frac{2\pi}{Z_i e m_i^2} \int_0^\infty d\mu \int_{-\infty}^\infty d\mathcal{P}_\varphi \sum_k \int_{\bar{H}_k^{\min}}^{\bar{H}_k^{\max}} d\bar{H} \oint d\varphi \times \int_0^{\tau_{\text{orb}}} d\tau (-\tilde{\mathbf{R}} \cdot \nabla F_i - \tilde{\mathbf{p}}_\parallel \partial_{p_\parallel} F_i + C_i + S_i - \partial_t F_i) \quad (16)$$

$$\doteq \Gamma_{\text{rem}} + \Gamma_{\text{col}} + \Gamma_s + \Gamma_t.$$

Here, the remainder flux  $\Gamma_{\text{rem}}$  is from  $-\tilde{\mathbf{R}} \cdot \nabla F_i - \tilde{\mathbf{p}}_\parallel \partial_{p_\parallel} F_i$ , the collisional flux  $\Gamma_{\text{col}}$  is from  $C_i$ , the source flux  $\Gamma_s$  is from  $S_i$ , and  $\Gamma_t$  is from  $-\partial_t F_i$ . Note that  $\Gamma_{\text{rem}}$  arises whenever the remainder Hamiltonian  $\tilde{H}$  is nonzero. This includes effects from turbulence, when  $\tilde{H}$  contains a nonaxisymmetric part. But  $\Gamma_{\text{rem}}$  can also include other effects. For example, in section 3.2.2,  $\tilde{H}$  varies poloidally but is still axisymmetric. Then, the corresponding  $\Gamma_{\text{rem}}$  describes effects from neoclassical processes rather than turbulence. Meanwhile, note that  $\Gamma_t \propto -\partial_t F_i$  is not a transport or source term *per se*; rather, a nonzero  $\Gamma_t$  is the result of transport and sources along the orbits.

To study steady-state transport and sources onto the loss orbits, we also define a loss-region function  $L(\mu, \mathcal{P}_\varphi, \bar{H})$ , such that  $L = 1$  for the loss orbits, which intersect the wall, and  $L = 0$  for the confined orbits, which do not intersect the wall. Then, by inserting  $L$  into the integrand of (16), we get the loss-orbit contribution to the flux; namely, the remainder flux can be decomposed as

$$\Gamma_{\text{rem}} = \Gamma_{\text{rem}}^{\text{loss}} + \Gamma_{\text{rem}}^{\text{conf}}, \quad (17)$$

and similarly for  $\Gamma_{\text{col}}$ ,  $\Gamma_s$ , and  $\Gamma_t$ . Finally, note that the above formulations apply to any closed flux surface, not just the LCFS. For example, in section 3 below, the formulations are applied to a core flux surface  $\psi_n = 0.4$ .

The orbit-flux formulation (16) has been numerically implemented in XGCa. A separate ion-orbit code has been developed [31], which describes the orbits  $(\bar{\mathbf{R}}(\tau), \bar{\mathbf{p}}_\parallel(\tau))$  labeled by  $(\mu, \mathcal{P}_\varphi, \bar{H})$ . Then,  $F_i^{\text{out}} - F_i^{\text{in}}$  is calculated in XGCa according to (15). And finally, the orbit flux is obtained from (14), where  $\oint d\varphi$  is replaced with  $2\pi$  for XGCa. The ion-orbit code also determines the loss-orbit region with the function  $L(\mu, \mathcal{P}_\varphi, \bar{H})$ , so

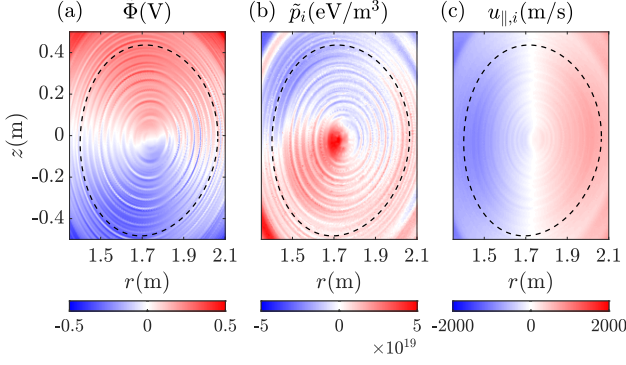


**Figure 2.** The nonzonal electrostatic potential perturbation  $\tilde{\Phi}$  (a), the nonzonal ion temperature perturbation  $\tilde{p}_i$  (b), and the ion fluid parallel velocity  $u_{\parallel,i}$  (c). The data is averaged over  $1.2\text{ms} < t < 1.6\text{ms}$  to reduce numerical noises. The black dashed curve shows the  $\psi_n = 0.4$  flux surface.

the loss-orbit contribution to the flux can be determined as in (17). To avoid repetitive XGCa simulations, we also made an alternative implementation where XGCa outputs  $F_i$ ,  $C_i$ , and  $S_i$ . Then, the orbit flux is calculated by a separate code [32].

### 3. Collisional relaxation of core $E_r$

In this section, we demonstrate the validity of our ion-orbit-flux diagnostic by studying the neoclassical  $E_r$  at a core flux surface  $\psi_n = 0.4$ . Results in this section are from the forward- $\nabla B$  configuration with  $B_\varphi < 0$ . Results for the backward- $\nabla B$  configuration are similar.

#### 3.1. Plasma properties at the quasisteady state

The initially Maxwellian distribution function does not correspond to a neoclassical equilibrium, so geodesic-acoustic-mode (GAM) oscillations occur. However, the GAM oscillations are quickly damped by viscosity and ion Landau damping, after which the system reaches a quasisteady state. Figure 2 shows the nonzonal potential perturbation  $\tilde{\Phi} \doteq \Phi - \langle \Phi \rangle$ , the nonzonal ion-pressure perturbation  $\tilde{p}_i \doteq p_i - \langle p_i \rangle$  where  $p_i \doteq \int d\mathcal{W}(\mu B + p_{\parallel}^2/2m_i)F_i$ , and the ion fluid parallel velocity  $u_{\parallel,i} \doteq \int d\mathcal{W}v_{\parallel}F_i / \int d\mathcal{W}F_i$  at the quasisteady state. Since we focus on the core flux surface  $\psi_n = 0.4$  in this section, we only show these field quantities around this surface. It is seen that both  $\tilde{\Phi}$  and  $\tilde{p}_i$  have up-down dipolar structures but they are out of phase, so the parallel electric field is against the ion parallel pressure gradient. Note that the nonzonal ion-density perturbation  $\tilde{n}_i$  is in phase with  $\tilde{\Phi}$  because of the adiabatic-electron model (7), assuming  $\tilde{n}_i \approx \tilde{n}_e$  in the core. Therefore,  $\tilde{n}_i$  and  $\tilde{p}_i$  are also out of phase, due to a large nonzonal ion-temperature perturbation out of phase with  $\tilde{n}_i$ . Meanwhile,  $u_{\parallel,i}$  has a left-right dipolar structure, so the plasma flows from the bottom

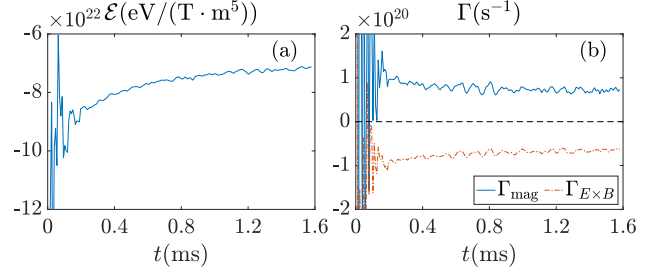


**Figure 3.** (a) The quantity  $\mathcal{E}$  (18) versus  $t$  at the  $\psi_n = 0.4$  flux surface. (b) The ion radial gyrocenter magnetic flux (blue solid curve) and  $\mathbf{E} \times \mathbf{B}$  flux (red dot-dashed curve) across the same flux surface. To reduce numerical fluctuations, the data has been smoothed by averaging over a time window of  $\Delta t = 0.04\text{ms}$ .

( $z < 0$ ) to the top ( $z > 0$ ). Such  $u_{\parallel,i}$  causes a density buildup at the top, but the perpendicular flow makes the total plasma flow divergence-free.

Since  $E_r = -\nabla\Phi \cdot \nabla\psi/|\nabla\psi|$  is not a flux function, we look at the following quantity

$$\mathcal{E}(\psi, t) \doteq -en_{i0}\partial_\psi \langle \Phi \rangle, \quad (18)$$

which can be considered as the radial electric force on ions from the zonal  $E_r$ . In the following, we use  $E_r$  and  $\mathcal{E}$  interchangeably. Figure 3(a) shows the time evolution of  $\mathcal{E}$  at the  $\psi_n = 0.4$  surface. After the initial GAM oscillations,  $\mathcal{E}$  goes through a slower collisional damping process until it relaxes to its neoclassical value. From the gyrokinetic Poisson equation (6), the zonal  $E_r$  is determined by the volume-integrated  $\hat{J}_0\delta n_i$ . Therefore, from the continuity relation, the ion radial gyrocenter flux must also vanish as  $\mathcal{E}$  approaches a constant value. Let us separate the radial flux into the magnetic-drift part and the  $\mathbf{E} \times \mathbf{B}$ -drift part:

$$\int d\mathbf{S} \cdot \int d\mathcal{W} F_i \dot{\mathbf{R}} = \Gamma_{\text{mag}} + \Gamma_{\mathbf{E} \times \mathbf{B}}, \quad (19)$$

where  $\Gamma_{\text{mag}} \doteq \int d\mathbf{S} \cdot \int d\mathcal{W} B_{\parallel}^{*-1} F_i (\hat{\mathbf{b}} \times \mu \nabla B / e + v_{\parallel} \mathbf{B}^*)$  and  $\Gamma_{\mathbf{E} \times \mathbf{B}} \doteq \int d\mathbf{S} \cdot \int d\mathcal{W} B_{\parallel}^{*-1} F_i (\hat{\mathbf{b}} \times \nabla \hat{J}_0 \Phi)$ . Figure 3(b) shows that  $\Gamma_{\text{mag}} > 0$  and  $\Gamma_{\mathbf{E} \times \mathbf{B}} < 0$  at the quasisteady state, such that the total flux is zero. These results are consistent with the dipolar structures of  $\tilde{p}_i$  and  $\tilde{\Phi}$  shown in figure 2. Namely, since  $\tilde{p}_i > 0$  at  $z < 0$  and the magnetic drift points in the negative- $z$  direction, the net magnetic flux is radially outward,  $\Gamma_{\text{mag}} > 0$ . Meanwhile, the  $\mathbf{E} \times \mathbf{B}$  drift points in the negative- $r$  direction, and is stronger at the outboard side ( $\theta \approx 0$ ) than the inboard side ( $\theta \approx \pi$ ); hence, the net  $\mathbf{E} \times \mathbf{B}$  flux is radially inward,  $\Gamma_{\mathbf{E} \times \mathbf{B}} < 0$ .

#### 3.2. Ion-orbit-flux diagnostic results

Below, we show the orbit-flux diagnostic results using two different orbit Hamiltonians:  $\bar{H} = \bar{H}_1 \doteq p_{\parallel}^2/2m_i + \mu B + \hat{J}_0 e \Phi$  (section 3.2.1) and  $\bar{H} = \bar{H}_2 \doteq p_{\parallel}^2/2m_i +$

$\mu B + \hat{J}_0 e \langle \Phi \rangle$  (section 3.2.2). With  $\bar{H} = \bar{H}_1$ , we will show that the results of  $\Gamma_{\text{col}}$  and  $\Gamma_t$  are consistent with the collisional relaxation of  $E_r$ . With  $\bar{H} = \bar{H}_2$ , the orbit flux also contains  $\Gamma_{\text{rem}}$  due to the nonzero  $\bar{H} = H - \bar{H}$ , and its physical meaning will be explained. The source flux  $\Gamma_s$  will not be considered, since  $S_i$  is set to zero in the simulation.

**3.2.1. Results with  $\bar{H} = \bar{H}_1$ .** Since  $\bar{H}_1 = p_{\parallel}^2/2m_i + \mu B + \hat{J}_0 e \Phi$  equals the true Hamiltonian  $H$ , the orbit characteristics  $\tilde{\mathbf{R}} = \tilde{\mathbf{R}}_1$  (governed by (8)) are the same as the true characteristics  $\tilde{\mathbf{R}}$  (governed by (1)). Then, comparing (16) and (19), the orbit flux is

$$\int d\mathbf{S} \cdot \int d\mathcal{W} F_i \tilde{\mathbf{R}}_1 = \Gamma_{\text{mag}} + \Gamma_{E \times B} = \Gamma_{\text{col}}^1 + \Gamma_t^1, \quad (20)$$

where we put a superscript “1” on  $\Gamma_{\text{col},t}$  to indicate that they are evaluated along  $\mathbf{R} = \tilde{\mathbf{R}}_1$ . Since  $\mathcal{E} < 0$  and  $|\mathcal{E}|$  decreases during the collisional relaxation (figure 3(a)), the net radial flux is negative, so we expect  $\Gamma_{\text{col}}^1 + \Gamma_t^1$  to be negative. This expectation is confirmed by the results shown in figure 4(a). The collisional flux  $\Gamma_{\text{col}}^1$  is negative, corresponding to a radially inward current induced by viscosity. The term  $\Gamma_t^1$  is positive, but the net radial flux  $\Gamma_{\text{col}}^1 + \Gamma_t^1$  is negative and damps to zero, consistent with the collisional relaxation of  $\mathcal{E}$ .

**3.2.2. Results with  $\bar{H} = \bar{H}_2$ .** To further explore the formulation, we can alternatively choose  $\bar{H} = \bar{H}_2 \doteq p_{\parallel}^2/2m_i + \mu B + \hat{J}_0 e \langle \Phi \rangle$ , which only includes the zonal part of  $\Phi$ . Since  $\bar{H}_2 \neq H$ , the orbit characteristics  $\tilde{\mathbf{R}} = \tilde{\mathbf{R}}_2$  (governed by (8)) are different from the true characteristics  $\tilde{\mathbf{R}}$  (governed by (1)). Specifically, the magnetic drifts in  $\tilde{\mathbf{R}}_2$  and  $\tilde{\mathbf{R}}$  are the same, but the  $\mathbf{E} \times \mathbf{B}$  drift in  $\tilde{\mathbf{R}}_2$  is always tangent to flux surfaces (assuming  $\hat{J}_0 \approx 1$  in the core). Therefore, the  $\mathbf{E} \times \mathbf{B}$ -drift contribution to the orbit flux vanishes, leaving only the magnetic-drift contribution:

$$\int d\mathbf{S} \cdot \int d\mathcal{W} F_i \tilde{\mathbf{R}}_2 = \Gamma_{\text{mag}} = \Gamma_{\text{rem}} + \Gamma_{\text{col}}^2 + \Gamma_t^2. \quad (21)$$

Here,  $\Gamma_{\text{rem}}$  comes from the remainder Hamiltonian  $\bar{H} = H - \bar{H}_2 \approx e\tilde{\Phi}$ . For emphasis, the nonzonal potential  $\tilde{\Phi}$  varies along the poloidal direction, but is still axisymmetric. We put a superscript “2” on  $\Gamma_{\text{col},t}$  to indicate that they are evaluated along  $\mathbf{R} = \tilde{\mathbf{R}}_2$ , which is different from  $\tilde{\mathbf{R}}_1$  since  $\bar{H}_2 \neq \bar{H}_1$ .

Figure 4(b) shows the orbit-flux diagnostic results with  $\bar{H} = \bar{H}_2$ . Because  $e\tilde{\Phi} \ll T_{i0}$  in the core (figures 1(d) and 2(a)), the difference between  $\bar{H}_1$  and  $\bar{H}_2$  is tiny, and  $\tilde{\mathbf{R}}_1$  and  $\tilde{\mathbf{R}}_2$  are almost identical. Consequently, there is no visible difference between  $\Gamma_{\text{col},t}^2$  in figure 4(b) and  $\Gamma_{\text{col},t}^1$  in figure 4(a). With  $\Gamma_{\text{col},t}^1 \approx \Gamma_{\text{col},t}^2$ , and by comparing (20) and (21), we expect  $\Gamma_{\text{rem}} \approx -\Gamma_{E \times B}$ . This expectation is also

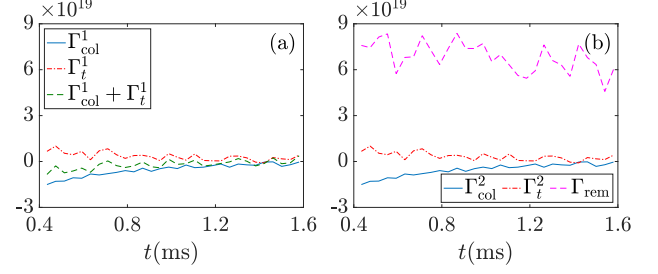


**Figure 4.** The orbit fluxes (in units  $\text{s}^{-1}$ ) at the  $\psi_n = 0.4$  surface, with two different choices of the orbit Hamiltonian: (a)  $\bar{H} = \bar{H}_1$  (section 3.2.1), and (b)  $\bar{H} = \bar{H}_2$  (section 3.2.2). In (a), shown are  $\Gamma_{\text{col}}^1$  (blue solid curve),  $\Gamma_t^1$  (red dot-dashed curve), and the sum of the two terms (green dashed curve). In (b), shown are  $\Gamma_{\text{col}}^2$  (blue solid curve),  $\Gamma_t^2$  (red dot-dashed curve), and  $\Gamma_{\text{rem}}$  (magenta dashed curve).

confirmed by the results shown in figure 4(b), namely,  $\Gamma_{\text{rem}} \approx 7 \times 10^{19} \text{s}^{-1}$  is approximately the same as  $-\Gamma_{E \times B}$  in figure 3(b).

We found that most of  $\Gamma_{\text{rem}}$  comes from the acceleration term  $-\tilde{p}_{\parallel} \partial_{p_{\parallel}} F_i$ , while the advection term  $-\tilde{\mathbf{R}} \cdot \nabla F_i$  is small and fluctuates around zero. This finding is consistent with the ordering estimate that  $\tilde{\mathbf{R}} \cdot \nabla F_i \sim E_{\theta} F_i / BL$  and  $\tilde{p}_{\parallel} \partial_{p_{\parallel}} F_i \sim e E_{\theta} B_{\theta} F_i / m_i v_t B$ , so the ratio between the two terms is  $\rho_{i\theta} / L$ , which is very small in the core. Here,  $L$  is an equilibrium length scale,  $v_t$  is ions’ thermal speed, and  $\rho_{i\theta} \doteq m_i v_t / e B_{\theta}$  is the poloidal gyroradius. For emphasis, this ordering is specific to our axisymmetric  $\tilde{\Phi}$  in the core, and would not hold if  $\tilde{\Phi}$  contains turbulent fluctuations.

The fact that  $\Gamma_{\text{rem}} \approx -\Gamma_{E \times B}$  is nontrivial. Both fluxes stem from the nonzero  $\bar{H} \approx e\tilde{\Phi}$ , but  $\Gamma_{E \times B}$  is evaluated at the surface, while  $\Gamma_{\text{rem}}$  is evaluated along the orbits. Further, since  $\Gamma_{\text{mag}} + \Gamma_{E \times B} \approx 0$  in steady state, we have  $\Gamma_{\text{mag}} \approx \Gamma_{\text{rem}}$ . Recalling (15) and (12), this reveals that the steady-state positive  $\Gamma_{\text{mag}}$  is supported by the acceleration from the parallel electric field  $E_{\parallel} = -\hat{\mathbf{b}} \cdot \nabla \tilde{\Phi}$ . Specifically, since the magnetic drift points in the negative- $z$  direction, orbits’ incoming points are at the top of the flux surface and the outgoing points are at the bottom. Co-current ions ( $v_{\parallel} > 0$ ) move counterclockwise to the inboard side where  $E_{\parallel} > 0$ , so the corresponding parallel acceleration term  $-\tilde{p}_{\parallel} \partial_{p_{\parallel}} F_i$  is positive, assuming  $\partial_{p_{\parallel}} F_i < 0$  at  $v_{\parallel} > 0$ . Similarly, counter-current ions ( $v_{\parallel} < 0$ ) move to the outboard side where  $E_{\parallel} < 0$ , so  $-\tilde{p}_{\parallel} \partial_{p_{\parallel}} F_i$  is also positive for them. Therefore,  $\tilde{p}_i > 0$  at the bottom (figure 2(b)) and the net magnetic-drift flux is positive,  $\Gamma_{\text{mag}} > 0$ .

#### 4. Effects of ion orbit loss on edge $E_r$

In this section, the orbit-flux diagnostic is used to study the effects of ion orbit loss on the edge  $E_r$ . Results



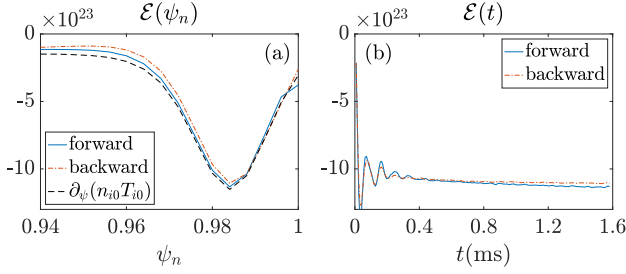


**Figure 5.** (a)  $\mathcal{E}$  versus  $\psi_n$  at  $t = 1.6$ ms from the forward- $\nabla B$  (blue solid curve) and the backward- $\nabla B$  configuration (red dot-dashed curve). Also shown is the radial ( $\psi$ ) gradient of the equilibrium ion pressure (black dashed curve). (b)  $\mathcal{E}$  at  $\psi_n = 0.984$  versus  $t$  from the two configurations.

from the forward- and backward- $\nabla B$  configurations are compared. It is found that while  $E_r$  remains quasisteady at the edge, there are persistent toroidal-rotation accelerations. Consequently, both  $\Gamma_{\text{col}}$  and  $\Gamma_t$  are nonzero but they cancel each other. The loss-orbit contribution to the flux,  $\Gamma_r^{\text{loss}}$ , is found to be small and cannot drive  $E_r$  significantly away from its neoclassical value. Hence, the difference in  $E_r$  in quasisteady state between the forward- and backward- $\nabla B$  configurations cannot be explained with ion orbit loss, for the given plasma parameters.

#### 4.1. Ion-orbit-flux diagnostic results

Figure 5 shows  $\mathcal{E}$  at the edge. A large  $|\mathcal{E}|$  is developed inside the LCFS, which balances the radial pressure gradient caused by the density pedestal shown in figure 1(c). For the forward- $\nabla B$  case, the peak of  $|\mathcal{E}|$  slowly increases over time (figure 5 (b)) in quasisteady state, while for the backward- $\nabla B$  case the increase is less pronounced. The slow increase of  $|\mathcal{E}|$  for the forward- $\nabla B$  case indicates a small radially outward flux, which is estimated to be  $\Gamma_r \approx 10^{19}\text{s}^{-1}$ ; for the backward- $\nabla B$  case,  $\Gamma_r$  is even smaller.

For the orbit-flux diagnostic, we choose  $\bar{H} = H$  so the orbit fluxes consist of  $\Gamma_{\text{col}}$  and  $\Gamma_t$ . The loss-orbit contribution to the fluxes is also calculated using the loss-region function  $L$ , which is numerically determined by the ion-orbit code [31]. The loss orbits make up about 30% of all the orbits considered, i.e.,  $\int L d\mu d\mathcal{P}_\varphi d\bar{H} / \int d\mu d\mathcal{P}_\varphi d\bar{H} \approx 0.3$ . This percentage is the same for both the forward- and backward- $\nabla B$  configurations, since the two cases have the same magnetic-field topology and similar levels of  $E_r$ . We have also verified that the shape of the loss region from our numerical  $L$  (not shown) is consistent with some earlier analytic studies [33, 34, 11].

Figure 6 shows the orbit-flux diagnostic results at the LCFS ( $\psi_n = 1$ ). Unlike the core (figure 4), here at the edge  $\Gamma_{\text{col}}$  and  $\Gamma_t$  do not vanish in quasisteady state. Instead,  $\Gamma_{\text{col}} > 0$  and  $\Gamma_t < 0$ , and their

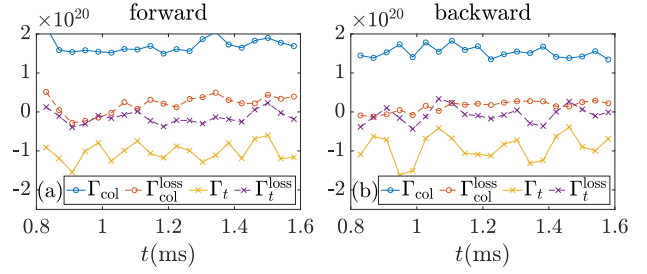


**Figure 6.** The orbit-flux diagnostic results at the LCFS. Shown are the results of  $\Gamma_{\text{col}}$  (circles) and  $\Gamma_t$  (crosses) for the forward- $\nabla B$  (a) and the backward- $\nabla B$  configurations (b). The solid curves are the total fluxes including all orbits, while the dashed curves are contributions from the loss orbits alone.

magnitudes ( $\approx 10^{20}\text{s}^{-1}$ ) are much larger compared to the actual radial flux  $\Gamma_r \approx 10^{19}\text{s}^{-1}$ , but the total orbit flux  $\Gamma_{\text{col}} + \Gamma_t$  is much smaller. Similarly, for the loss-orbit contribution,  $\Gamma_{\text{col}}^{\text{loss}} > 0$  and  $\Gamma_t^{\text{loss}} < 0$ . Due to the cancellation between  $\Gamma_{\text{col}}^{\text{loss}}$  and  $\Gamma_t^{\text{loss}}$ , the net loss-orbit flux appears to be small, and is estimated to be  $\Gamma_r^{\text{loss}} \approx 10^{19}\text{s}^{-1}$ . These results are similar between the forward- $\nabla B$  (figure 6(a)) and the backward- $\nabla B$  (figure 6(b)) configurations.

#### 4.2. Effects of $\Gamma_r^{\text{loss}}$ on $E_r$

Let us integrate the gyrokinetic Poisson equation (6) over the volume inside the LCFS. From Gauss's law, we have

$$\int \frac{n_{i0}m_i}{eB^2} E_r dS = \int \hat{j}_0 \delta n_i dV, \quad (22)$$

where  $dS = |d\mathbf{S}|$  and  $dV$  is the volume element. Since the right-hand side of (22) is approximately the perturbation of number of ions inside the LCFS, we take the time derivative of (22) and use the continuity equation. This gives a relation between the ion radial gyrocenter flux and the radial electric field:

$$\Gamma_r \approx -\frac{\partial}{\partial t} \int \frac{n_{i0}m_i}{eB^2} E_r dS. \quad (23)$$

(The electron radial flux is zero due to the adiabatic-electron assumption.) We can further separate  $\Gamma_r$  into the confined-orbit contribution and the loss-orbit contribution,  $\Gamma_r = \Gamma_r^{\text{conf}} + \Gamma_r^{\text{loss}}$ . Without orbit loss,  $\Gamma_r = \Gamma_r^{\text{conf}}$ , and  $E_r$  approaches its neoclassical value at steady states,

$$\Gamma_r^{\text{conf}}(E_r^{\text{neo}}) = 0. \quad (24)$$

Suppose a nonzero  $\Gamma_r^{\text{loss}}$  leads to  $E_r = E_r^{\text{neo}} + \Delta E_r$  in steady state. We then have

$$\Gamma_r^{\text{conf}}(E_r^{\text{neo}} + \Delta E_r) = -\Gamma_r^{\text{loss}}. \quad (25)$$

For simplicity, let us assume that  $\Gamma_r^{\text{conf}}$  approximately damps  $E_r$  towards  $E_r^{\text{neo}}$  with a constant neoclassical

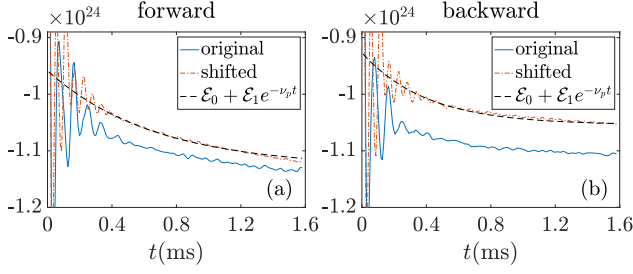


**Figure 7.** Comparisons of  $\mathcal{E}$  (in units  $\text{eV}/(\text{T} \cdot \text{m}^5)$ ) between simulations using the original equilibrium profile (blue solid curves) and the radially shifted profile (red dot-dashed curves). For the original profile,  $\mathcal{E}$  is evaluated at  $\psi_n = 0.984$ ; and for the shifted profile,  $\mathcal{E}$  is evaluated at  $\psi_n = 0.884$ . To reduce numerical fluctuations, the data has been smoothed by averaging over a time window of  $\Delta t = 0.04 \text{ ms}$ . Also shown are fitting curves  $\mathcal{E} = \mathcal{E}_0 + \mathcal{E}_1 e^{-\nu_p t}$  that model the collisional relaxation. In (a),  $\mathcal{E}_0 = -1.13 \times 10^{24}$ ,  $\mathcal{E}_1 = 1.71 \times 10^{23}$ , and  $\nu_p = 1.5 \times 10^3 \text{ s}^{-1}$ . In (b),  $\mathcal{E}_0 = -1.05 \times 10^{24}$ ,  $\mathcal{E}_1 = 1.28 \times 10^{23}$ , and  $\nu_p = 2.5 \times 10^3 \text{ s}^{-1}$ .

collisional damping rate  $\nu_p$ . Then, from (23) and (25),  $\Delta E_r$  is estimated from the following relation:

$$\nu_p \int \frac{n_{i0} m_i}{e B^2} \Delta E_r dS \approx -\Gamma_r^{\text{loss}}. \quad (26)$$

To estimate  $\nu_p$  without the effects from ion orbit loss, we ran XGCa simulations again, but with the equilibrium profile of  $n_{i0}$  and  $T_{i0}$  radially shifted inwards by  $\Delta\psi_n = 0.1$ . Figure 7 shows a comparison of  $E_r$  between the simulations with the original profile and the shifted profile, and  $E_r$  behaves similarly for the two profiles, suggesting that the slow increase of  $|E_r|$  for the forward- $\nabla B$  case is not because of complicated effects near the LCFS, such as ion orbit loss. By fitting the numerical results to an analytic form  $\mathcal{E} = \mathcal{E}_0 + \mathcal{E}_1 e^{-\nu_p t}$ , we estimate  $\nu_p \approx 1.5 \times 10^3 \text{ s}^{-1}$  for the forward- $\nabla B$  case, and  $\nu_p \approx 2.5 \times 10^3 \text{ s}^{-1}$  for the backward- $\nabla B$  case (figure 7). Both estimates of  $\nu_p$  are on the same order of magnitude with the local ion-ion collision rate  $\nu_i \approx 1.6 \times 10^3 \text{ s}^{-1}$ , which is calculated using  $n_{i0} \approx 10^{19} \text{ m}^{-3}$  and  $T_{i0} \approx 200 \text{ eV}$  at the edge [35]. Assuming  $\nu_p = 1.5 \times 10^3 \text{ s}^{-1}$ , together with  $\Gamma_r^{\text{loss}} \approx 10^{19} \text{ s}^{-1}$  and  $\int \hat{j}_0 \delta n_i dV \approx 3 \times 10^{17}$ , we estimate the relative change of  $E_r$  as

$$\left| \frac{\Delta E_r}{E_r} \right| \approx \left| \frac{\Gamma_r^{\text{loss}}}{\nu_p \int \hat{j}_0 \delta n_i dV} \right| \approx 2.2\%. \quad (27)$$

This is consistent with figure 7, in which  $\mathcal{E}$  for the shifted profiles is within a few percent of  $\mathcal{E}$  for the original profiles, although the shifted-profile calculations involve almost no loss orbits. For these simulations, we thus conclude that  $\Gamma_r^{\text{loss}}$  is too small to drive  $E_r$  significantly away from its neoclassical value. Difference in  $E_r$  is observed between the forward- and backward- $\nabla B$  configurations, but such difference is not caused by ion orbit loss, since the  $E_r$  profiles also differ in the shifted-profile simulations (figure 7).

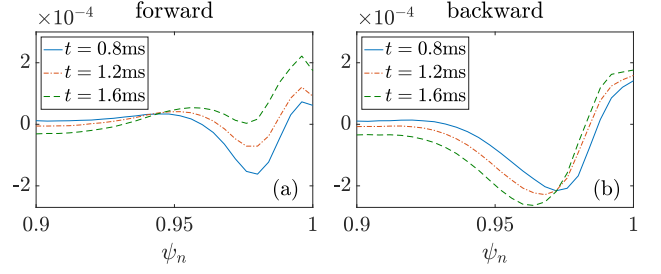


**Figure 8.** Time evolution of the flux-surface averaged toroidal angular momentum density (in units  $\text{kg}/(\text{m} \cdot \text{s})$ ) at the edge.

#### 4.3. Toroidal-rotation acceleration at the edge

The fact that  $\Gamma_t$  is nonzero indicates that  $F_i$  is changing over time, even though the flux-surface averaged density is quasisteady. Since the lowest-order moment (density) of  $F_i$  is not changing, we will look for effects of the change of  $F_i$  on its next-order moment, i.e., the velocity. Figure 8 shows the flux-surface averaged toroidal angular momentum density  $\langle \int dW F_i p_{\parallel} R B_{\varphi} / B \rangle$  at the edge. Because  $B_{\theta} > 0$ , the equilibrium plasma current is oppositely directed to  $\nabla\varphi$ , so a positive (negative) toroidal angular momentum corresponds to a counter- (co-)current rotation. As shown in the figure, the toroidal rotation has a co-current peak inside the LCFS, consistent with previous results [24, 26, 30]. As time progresses, there is counter-current acceleration just inside the LCFS ( $\psi_n \gtrsim 0.97$ ) for both configurations. As one moves further inside radially ( $\psi_n \lesssim 0.96$ ), the acceleration shifts to the co-current direction. Both the toroidal-rotation velocity and acceleration are much stronger at the outboard than at the inboard.

The counter-current toroidal acceleration just inside the LCFS is consistent with the negative  $\Gamma_t$ . Counter-current acceleration at fixed density implies an increase of counter-current ions and a decrease of co-current ions. At the outboard midplane, where the acceleration is concentrated, most co-current ions are on orbits that remain inside the LCFS, which do not contribute to the orbit flux. Many counter-current ions are on orbits that do cross the LCFS, thus the counter-current acceleration results in a net positive  $\partial_t F_i$  in (16), which corresponds to a negative  $\Gamma_t$ .

For electrostatic simulations with the adiabatic-electron model (7), the toroidal angular momentum is conserved [36, 37]. Although the toroidal angular momentum consists of both a parallel-momentum portion (shown in figure 8) and an  $\mathbf{E} \times \mathbf{B}$  portion, the latter is almost constant in time as  $E_r$  is quasisteady. Therefore, the observed toroidal-rotation acceleration indicates a nonzero radial toroidal angular momentum flux. In other words, there is a nondiffusive momentum flux at the edge. The peak of the toroidal rotation



is at the outboard midplane, suggesting that trapped ions may play a significant role. The observed counter-current rotation acceleration near the LCFS is also consistent with the toroidal  $\mathbf{E} \times \mathbf{B}$ -drift direction at the outboard side. All of these observations are of interest for future studies.

## 5. Conclusions

The ion-orbit-flux formulation [20, 21] has been implemented as a numerical diagnostic in XGCa [19, 31, 32]. The diagnostic measures the separate contributions to the ion orbit loss from different transport mechanisms and sources. The validity of the diagnostic is demonstrated by studying the collisional relaxation of  $E_r$  in the core. Then, the diagnostic is used to study effects of ion orbit loss on  $E_r$  at the edge of a DIII-D H-mode plasma. In quasisteady state, the edge  $E_r$  is found to be mainly determined by the radial ion force balance condition, in which the radial electric force on ions balances the large ion pressure gradient associated with the given density pedestal. In this quasisteady state, the collisional loss-orbit flux of ion gyrocenters cannot drive  $E_r$  significantly away from its neoclassical value.

## Acknowledgments

This work was supported by the U.S. Department of Energy through Contract No. DE-AC02-09CH11466. The simulations presented in this article were performed on computational resources managed and supported by Princeton Research Computing, a consortium of groups including the Princeton Institute for Computational Science and Engineering (PICSciE) and the Office of Information Technology's High Performance Computing Center and Visualization Laboratory at Princeton University. This research used resources of the National Energy Research Scientific Computing Center, which is supported by the Office of Science of the U.S. Department of Energy under Contract No. DE-AC02-05CH11231.

## Data Availability

Digital data can be found in DataSpace of Princeton University [38].

## References

- [1] Itoh S I and Itoh K 1988 *Physical Review Letters* **60** 2276
- [2] Shaing K C and Crume Jr E 1989 *Physical Review Letters* **63** 2369
- [3] Connor J and Wilson H 2000 *Plasma Physics and Controlled Fusion* **42** R1
- [4] Stacey W M 2011 *Physics of Plasmas* **18** 102504
- [5] Stoltzfus-Dueck T 2012 *Physical Review Letters* **108** 065002
- [6] Battaglia D, Burrell K, Chang C, Ku S, Degraessie J and Grierson B 2014 *Physics of Plasmas* **21** 072508
- [7] Boedo J, DeGrassie J, Grierson B, Stoltzfus-Dueck T, Battaglia D, Rudakov D, Belli E, Groebner R, Hollmann E, Lasnier C *et al.* 2016 *Physics of Plasmas* **23** 092506
- [8] Chang C, Ku S, Tynan G, Hager R, Churchill R, Cziegler I, Greenwald M, Hubbard A and Hughes J 2017 *Physical Review Letters* **118** 175001
- [9] Ku S, Chang C, Hager R, Churchill R, Tynan G, Cziegler I, Greenwald M, Hughes J, Parker S E, Adams M *et al.* 2018 *Physics of Plasmas* **25** 056107
- [10] Brzozowski III R W, Jenko F, Bilato R, Cavedon M and Team A U 2019 *Physics of Plasmas* **26** 042511
- [11] DeGrassie J, Groebner R, Burrell K and Solomon W 2009 *Nuclear Fusion* **49** 085020
- [12] deGrassie J S, Boedo J A and Grierson B A 2015 *Physics of Plasmas* **22** 080701
- [13] Pan C, Wang S and Ou J 2014 *Nuclear Fusion* **54** 103003
- [14] Chang C S, Kue S and Weitzner H 2002 *Physics of Plasmas* **9** 3884–3892
- [15] Shaing K 2002 *Physics of Plasmas* **9** 1–3
- [16] Ku S, Baek H and Chang C S 2004 *Physics of plasmas* **11** 5626–5633
- [17] Shaing K C 1992 *Physics of Fluids B: Plasma Physics* **4** 171–175
- [18] Shaing K C 1992 *Physics of Fluids B: Plasma Physics* **4** 3310–3315
- [19] See <https://www.osti.gov/doecode/biblio/12570> for more details about the code XGC.
- [20] Stoltzfus-Dueck T 2020 *Nuclear Fusion* **60** 016031
- [21] Stoltzfus-Dueck T and Zhu H 2021 *Plasma Physics and Controlled Fusion* **63** 115001
- [22] Müller S, Boedo J, Burrell K, DeGrassie J, Moyer R, Rudakov D and Solomon W 2011 *Physical review letters* **106** 115001
- [23] Müller S, Boedo J, Burrell K, Degraessie J, Moyer R, Rudakov D, Solomon W and Tynan G 2011 *Physics of Plasmas* **18** 072504
- [24] Seo J, Chang C, Ku S, Kwon J, Choe W and Müller S H 2014 *Physics of Plasmas* **21** 092501
- [25] Zhang F, Hager R, Ku S H, Chang C S, Jardin S C, Ferraro N M, Seol E S, Yoon E and Shephard M S 2016 *Engineering with Computers* **32** 285–293
- [26] Chang C S, Ku S and Weitzner H 2004 *Physics of Plasmas* **11** 2649–2667
- [27] Ku S, Hager R, Chang C S, Kwon J and Parker S E 2016 *Journal of Computational Physics* **315** 467–475
- [28] Yoon E and Chang C 2014 *Physics of Plasmas* **21** 032503
- [29] Hager R, Yoon E, Ku S, D'Azevedo E F, Worley P H and Chang C S 2016 *Journal of Computational Physics* **315** 644–660
- [30] Chang C S and Ku S 2008 *Physics of Plasmas* **15** 062510
- [31] Contact the authors for more details about the ion-orbit code.
- [32] Contact the authors for more details about the orbit-flux code.
- [33] Chankin A and McCracken G 1993 *Nuclear Fusion* **33** 1459
- [34] Miyamoto K 1996 *Nuclear Fusion* **36** 927
- [35] Huba J D 2004 Revised *NRL plasma formulary* (Naval Research Laboratory)
- [36] Scott B and Smirnov J 2010 *Physics of Plasmas* **17** 112302
- [37] Stoltzfus-Dueck T and Scott B 2017 *Nuclear Fusion* **57** 086036
- [38] See <https://dataspace.princeton.edu/handle/88435/dsp01pz50gz45g> for the digital data.